coatings

Article

Electrodeposition of a Ni–P–TiO_2/$Ti_3C_2T_x$ Coating with In Situ Grown Nanoparticles TiO_2 on $Ti_3C_2T_x$ Sheets

Yingchao Du [1,2], Xiaomeng Zhang [1], Lianqi Wei [1], Bo Yu [1,2], Daqing Ma [3,*] and Shufeng Ye [1,*]

[1] State Key Laboratory of Multiphase Complex Systems, Institute of Process Engineering, Chinese Academy of Sciences, Beijing 100190, China; ycdu@ipe.ac.cn (Y.D.); xmzhang@ipe.ac.cn (X.Z.); lqwei@ipe.ac.cn (L.W.); yubo@ipe.ac.cn (B.Y.)

[2] School of Chemical Engineering, University of Chinese Academy of Sciences, Beijing 100049, China

[3] China Academy of Safety Science and Technology, Beijing 100012, China

[*] Correspondence: madq@chinasafety.ac.cn (D.M.); sfye@ipe.ac.cn (S.Y.); Tel.: +86-8491-1220 (D.M.); +86-8254-4899 (S.Y.)

Received: 14 October 2019; Accepted: 7 November 2019; Published: 12 November 2019

Abstract: Protective coatings have received considerable attention for the surface treatment of devices. Herein, in situ grown nanoparticles, TiO_2 on $Ti_3C_2T_x$ sheets (TiO_2/$Ti_3C_2T_x$), are prepared by a simple hydrothermal oxidation method possessing the layer structure, which is applied to prepare protective coatings. The Ni–P–TiO_2/$Ti_3C_2T_x$ coating is prepared by electroplating technology, revealing more excellent properties than those of the Ni–P coating. Compared with the Ni–P coating, even though the Ni–P–TiO_2/$Ti_3C_2T_x$ coating holds the rough surface, the wettability is changed from hydrophilic to hydrophobic, owing to the gathering existence of TiO_2/$Ti_3C_2T_x$ on the surface and coarse surface texture. In addition, the participation of TiO_2/$Ti_3C_2T_x$ in the Ni–P coating can improve the capacity of corrosion prevention and decrease the corrosion rate. According to the results of hardness and wear tests, microhardness of the Ni–P–TiO_2/$Ti_3C_2T_x$ coating is approximately 1350 kg mm^{-2} and the coefficient of friction (COF) of Ni–P–TiO_2/$Ti_3C_2T_x$ coatings is about 0.40, which is much lower than that of Ni–P coatings. Thus, the Ni–P–TiO_2/$Ti_3C_2T_x$ coating can be a promising material to protect the surface of equipment.

Keywords: TiO_2/$Ti_3C_2T_x$; Ni–P–TiO_2/$Ti_3C_2T_x$ coatings; microhardness; corrosion; wear

---

1. Introduction

It is well known that the surface is the most essential part of several engineering components, easily suffering from corrosion, abrasion, and fatigue [1,2]. Researchers have made great efforts to improve these surface properties, such as hardness, wear performance, and corrosion resistance [3,4]. Similarly, various technologies have been employed to prepare the protective coating, including electroplating, plasma thermal spray, and chemical vapor deposition [5]. Due to low cost and easy operation, electroplating is the most outstanding among these technologies [6–9].

According to previous papers, the Ni–P composite coating possesses excellent properties, so it is widely used to deal with problems in the engineering process [10,11]. However, when encountering some tricky conditions, the Ni–P composite coating is hardly able to overcome these difficulties [12]. Thus, the modification of Ni–P composite coatings is proven to be an efficient method to expand application fields, so introducing particles into these coatings can improve their properties, such as TiO_2 particles, MoS_2 particles, and Al_2O_3 particles [13–16]. Generally, the property of the composite coating is closely related to these incorporating particles [17].

Usually, two-dimensional (2D) structural materials hold a low friction coefficient, so they can show promising prospects in solid lubrication. As a typical layered structural material, $Ti_3C_2T_x$ particles have been applied to lubricating oil, owing to wear resistance, thermal stability, and electrochemical corrosion [18]. Due to the weak Van der Waal's bonding between layers, there is potential for $Ti_3C_2T_x$ particles to slide, so it holds a low friction coefficient of 0.1 in lubricating oil. Thus, these incorporating $Ti_3C_2T_x$ particles can provide a low friction coefficient for the Ni–P coating [19]. As previous papers have shown, TiO_2 particles introduced into coatings can increase the hardness, wear resistance, and corrosion resistance. Baghery et al. prepared the Ni–TiO_2 coating, which exhibited excellent properties of hardness and wear resistance [2]. Similarly, Uttam and Duchaniya synthesized the Ni–P–TiO_2 coating on mild steel, showing excellent corrosion resistance [20]. Therefore, it is a perfect idea for introducing TiO_2 particles into the Ni–P coating.

$TiO_2/Ti_3C_2T_x$ particles with heterogeneous interfaces have been widely used in photocatalytic activity and electrochemistry. In previous works, Xu et al. prepare in situ grown nanocrystal TiO_2 on 2D Ti_3C_2 nanosheets for artificial photosynthesis of chemical fuels [21]. Peng et al. found that hybrids of two-dimensional Ti_3C_2 and TiO_2 exposing {001} facets enhanced photocatalytic activity [22]. However, it is little reported that $TiO_2/Ti_3C_2T_x$ particles are used in the area of surface treatment. In this work, in situ grown nanocrystal TiO_2 on $Ti_3C_2T_x$ particles were prepared by hydrothermal reaction and incorporated into Ni–P coatings to prepare the Ni–P–$TiO_2/Ti_3C_2T_x$ coating. These particles can combine excellent properties with TiO_2 and $Ti_3C_2T_x$, so it is beneficial to improve the wear resistance and corrosion resistance of the Ni–P coating.

2. Experiment Procedure

2.1. Preparation of $TiO_2/Ti_3C_2T_x$ Powders

Ti_3AlC_2 powders (10 g) were transferred to a Teflon beaker, and 40 mL 40% hydrofluoric acid were dropwise added into them under stirring at 40 °C for 18 h. Then, these obtained products were washed with deionized water until a pH of 5 and dried in a vacuum drying oven at a temperature of 80 °C for 24 h [18].

Those as-prepared products (2.4 g) were added to a beaker, containing 360 mL 1M hydrochloric acid and 7.2 g sodium fluoroborate under agitation for 30 min. The obtained solution was shifted into hydrothermal reactors at 160 °C for 12 h. After washing with deionized water several times, these products were shifted to a vacuum drying oven at 80 °C for 24 h.

2.2. Preparation of Composite Coatings

$TiO_2/Ti_3C_2T_x$ powders (4 $g\cdot L^{-1}$) were dispersed uniformly into nickel sulfate plating baths, including nickel sulfate, nickel chloride, boric acid, citric acid, and SDS under stirring. The bath compositions and experimental conditions are shown in Table 1. A pure nickel plate (70 mm × 60 mm) and manganese steel (20 mm × 30 mm) were taken as the anode and cathode, respectively. The composition of the manganese steel is shown in Figure 1, mainly containing elements of Fe, Mn, Cr, Si, S, and P. After the process of electroplating, the composite coating was washed by ultrasound for 10 min, dried in an oven at 100 °C for 1 h, and then annealed in a tube furnace at 400 °C for 60 min under argon atmosphere.

2.3. Material Characterization

Field-emission scanning electron microscopy (FE-SEM, JEOL JSM-6700F, JEOL, Tokyo, Japan) and a transmission electron microscopy (TEM, JEOL JEM-2010F, JEOL, Tokyo, Japan) equipped with an accelerating voltage of 200 kV were employed to observe the morphology and structure of these samples. X-ray diffractometer (XRD, Philips, X'Pert Pro, Almelo, the Netherlands) with Cu-Kα radiation and X-ray fluorescence spectrometer (XRF; AXIOS-MAX, PANalytical B.V., Almelo, the Netherlands) were used to measure the chemical composition of samples. A laser-scanning Raman microscope

(Nanophoton Corporation, Raman-11, Osaka, Japan) was applied to detect the structure of samples with a confocal laser spectrometer, using the 532 nm excitation of the argon laser at room temperature. X-ray photoelectron spectroscopy (XPS, Themo Fisher Scientific, ESCALAB 250Xi, Waltham, MA, USA) with a monochromatic Al Kα radiation was used to record the surface analysis of $TiO_2/Ti_3C_2T_x$ powders. The Fourier transform infrared (FTIR, Excalibur 3100, Varian Medical Systems, Palo Alto, CA, USA) spectroscopy measurement was conducted in a KBr pellet at room temperature. A digital micro-hardness tester (MC010, Yanrui, Shanghai, China) was applied to determine the microhardness of composite coatings at a load of 300 g for 15 s, and the result was achieved from the average of five data on the sample surface. A surface roughness tester (TR211, Shidai Ruida, Beijing, China) was used to detect the Ra of composite coatings, which was obtained from the mean result of five data sets. An electrochemical station (UN-O-16076, Zahner, Kronach, Germany) was used to test the electrochemical measurement in a three-electrode system. Water contact angle measurements using 2 uL water droplets were determined by a measurement apparatus (K100, Kruss, Hamburg, Germany) at 25 °C with DropSnake to shape the drop and measure the contact angle. Wear tests were carried out by a circumrotating ball-on-disk tribometer (HT-1000, Lanzhou, China) with silicon nitride as the grinding material.

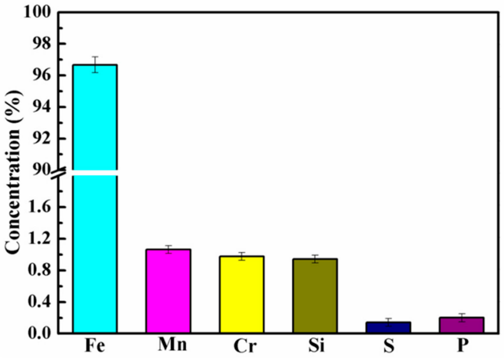

Figure 1. X-ray fluorescence (XRF) results of the composition for the manganese steel.

Table 1. Bath compositions and experimental conditions.

Compositions	Experimental Conditions
Nickel sulfate	250 g L^{-1}
Nickel chloride	40 g L^{-1}
Boric acid	40 g L^{-1}
Citric acid	45 g L^{-1}
Sodium hypophosphite	30 g L^{-1}
$TiO_2/Ti_3C_2T_x$ powders	4 g L^{-1}
SDS	1 g L^{-1}
pH	3–4
Current condition density	2 A dm^{-2}
Time	1 h
Temperature	50 °C
Magnetic stirring speed	600 rpm

3. Results and Discussions

3.1. Characterization of Powders

Figure 2 shows the XRD pattern of $TiO_2/Ti_3C_2T_x$ powders with TiO_2 and Ti_3AlC_2 standard patterns. Due to no information of $Ti_3C_2T_x$ in ICSD, a Ti_3AlC_2 standard pattern with the space group *P63/mmc* was used to fit the XRD pattern of $TiO_2/Ti_3C_2T_x$ powders [23]. These characteristic peaks located at 9.58° and 19.17° were assigned to (002) and (004), which shifted lower to 8.95° and 17.91°, indicating the existence of $Ti_3C_2T_x$. In addition, the shift of planes can show the increase of the c-lattice parameter and basal spacing. After hydrothermal oxidation, peaks belonging to anatase TiO_2 phase were much stronger than those of $Ti_3C_2T_x$ powders, demonstrating that $Ti_3C_2T_x$ was partly oxidized and the anatase TiO_2 was present on the $Ti_3C_2T_x$ [22].

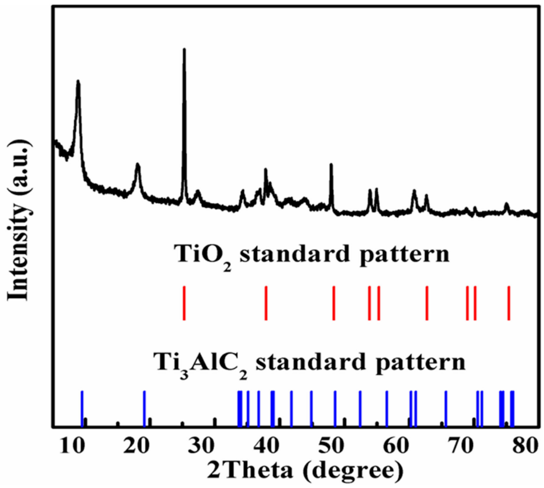

Figure 2. X-ray diffraction (XRD) pattern of $TiO_2/Ti_3C_2T_x$ powders with TiO_2 and Ti_3AlC_2 standard patterns.

Raman spectra and FTIR spectra of $TiO_2/Ti_3C_2T_x$ and $Ti_3C_2T_x$ powders are shown in Figure 3. In Figure 3a, the strongest peak located at 150 cm^{-1} is attributed to the symmetry vibration E_g of anatase TiO_2. Similarly, peaks of 413, 520, and 634 cm^{-1} are assigned to the vibration mode of B_{1g}, A_{1g}, and E_g of anatase TiO_2, separately [24,25]. According to the characteristic anatase Raman peak of pure TiO_2, a slight increase in the Eg1 peak is detected [26]. The peaks are in a tetragonum in Figure 3, showing the existence of TiO_2. These peaks of anatase TiO_2 mainly appear among 800~500 cm^{-1}, so peaks of $TiO_2/Ti_3C_2T_x$ are stronger than those of $Ti_3C_2T_x$. In addition, the peak located at ~570 cm^{-1} can be assigned to the deformation vibration of the Ti–O bond. [25] Thus, these results of Raman and FTIR spectra indicate the formation of anatase TiO_2.

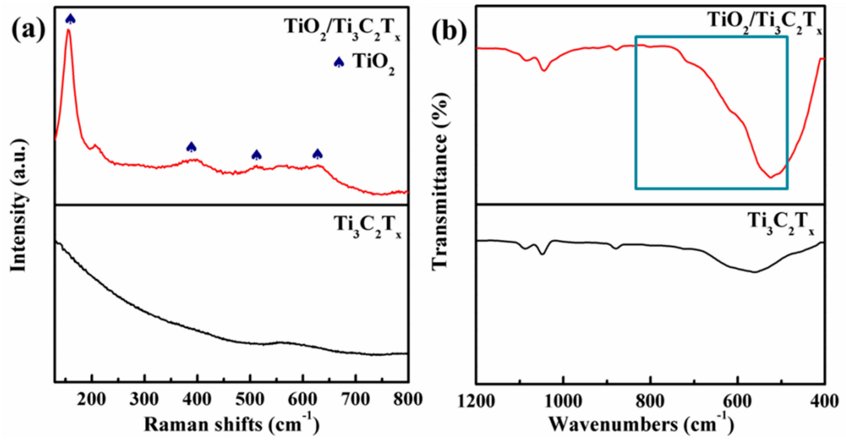

Figure 3. (**a**) Raman spectra and (**b**) Fourier transform infrared (FTIR) spectra of $TiO_2/Ti_3C_2T_x$ and $Ti_3C_2T_x$ powders.

SEM images of $Ti_3C_2T_x$ powders and $TiO_2/Ti_3C_2T_x$ powders with EDS elemental mapping are clearly seen in Figure 4. In Figure 4a, the layered structure of $Ti_3C_2T_x$ powders is obviously shown after the etching effect of HF solution. In Figure 4b, after the hydrothermal oxidation, even though anatase

TiO_2 particles exist on the $Ti_3C_2T_x$ powders, the layered structure of $Ti_3C_2T_x$ powders still remain, deriving from the titanium atoms on $Ti_3C_2T_x$, acting as nucleating sites for the growth of anatase TiO_2 [27]. The HRSEM image of the circle area displays the anatase TiO_2 with a thickness of ~30 nm and length of ~200 nm, and it can be observed that the interfacial angle between the {001} and {101} facets of anatase TiO_2 is about 68.3° [28]. As for the previous paper, the percentage of the {001} facets can be calculated as about 69.8% from the schematic diagram of an anatase TiO_2 [29]. The elemental mapping results from Figure 4c show that main elements of oxygen, titanium, and carbon are present on the $TiO_2/Ti_3C_2T_x$ powders, so it corresponds to results of the XRD pattern (Figure 2).

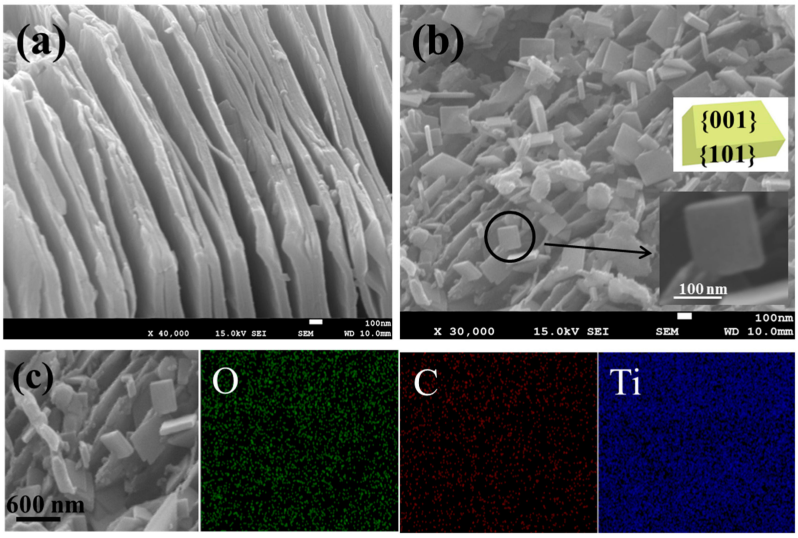

Figure 4. Scanning electron microscopy (SEM) images of (**a**) $Ti_3C_2T_x$ powders, (**b**) $TiO_2/Ti_3C_2T_x$ powders with insets of HRSEM image in the area of the black circle and schematic diagram of an anatase TiO_2 crystal, and (**c**) $TiO_2/Ti_3C_2T_x$ powders with EDS images.

In Figure 5, HRTEM images show the crystal relationship of TiO_2 and $Ti_3C_2T_x$. Figure 5a reveals the morphology of TiO_2 with a tetragonal shape, and Figure 5b shows the growth of TiO_2 derived from $Ti_3C_2T_x$. In Figure 5c, the interface between TiO_2 and $Ti_3C_2T_x$ can be clearly demonstrated by the yellow line. From Figure 5d, the result of FFT demonstrates the existence of anatase TiO_2 with crystal planes of (01-1) and (100), while it is clearly seen that the FFT result shows the presence of hexagonal $Ti_3C_2T_x$ with crystal planes of (006) and (103) in Figure 5e. Figure 5f shows that the seamless connection of TiO_2 and $Ti_3C_2T_x$ is due to the small discordance between {103} of $Ti_3C_2T_x$ and {11-1} of TiO_2 [22]. These results show that TiO_2 crystals are present on the crack of $Ti_3C_2T_x$ sheets, indicating that the nucleation of TiO_2 may exist at the defective positions of $Ti_3C_2T_x$. In addition, TiO_2 at the defect sites of $Ti_3C_2T_x$ may come from hydrated Ti^{3+} ions, which are from the titanium of $Ti_3C_2T_x$ [30,31].

From Figure 6, XPS spectra of Ti2p, C1s and O1s for $Ti_3C_2T_x$, and $TiO_2/Ti_3C_2T_x$ are clearly observed. In Figure 6a, the Ti2p spectra are traced to $Ti2p_{3/2}$ and $Ti2p_{1/2}$ with four pairs and each pair separation of 5.7 eV. These peaks of $Ti2p_{3/2}$ focused on 454.9, 455.8, 456.6, and 459.4 eV are attributed to Ti–C, Ti–X, Ti_xO_y, and TiO_2, respectively. In addition, the intensity of TiO_2 becomes strong and sharp after the hydrothermal oxidation attributed to TiO_2 (Ti ions in the valence of Ti^{4+}), while other peaks decrease, suggesting the formation of TiO_2 from $Ti_3C_2T_x$. As shown in Figure 6b, the C1s is fitted with five peaks, which are located at 281.6, 282.8, 284.8, 286.2, and 288.6 eV, assigned to Ti–C, C–Ti–O_a coming from the adsorbed –OH, C–C, C–O, and C–F, respectively. Due to the appearance of heterojunctions in MXene layers, the intensity of the peak is located at 281.6 eV. The hydrothermal oxidation reduces the appearance of C–Ti–O_b, derived from the interface of TiO_2 and $Ti_3C_2T_x$ powders [32]. As for the O1s spectra in Figure 6c, four peaks of 529.4, 530.4, 531.8, and 533.3 eV are taken for adsorbed O, Ti–O–Ti, Ti–OH, and C–OH, separately [33]. Thus, this further verifies the presence of TiO_2 transformed from $Ti_3C_2T_x$.

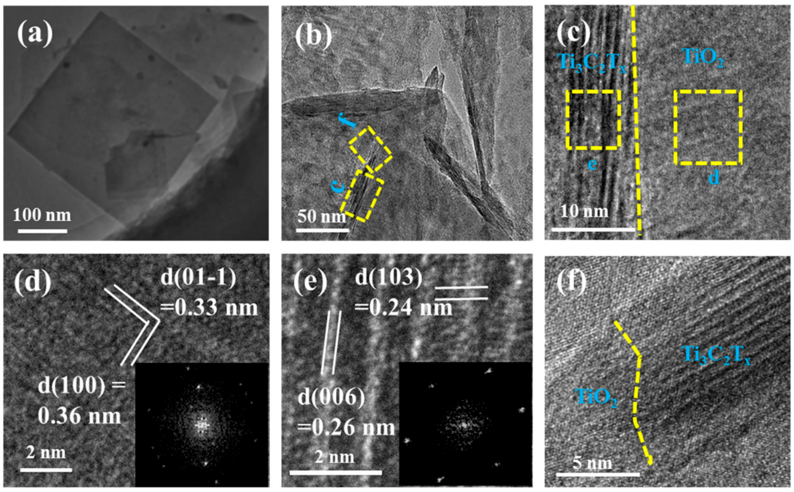

Figure 5. (**a**,**b**) TEM image of $TiO_2/Ti_3C_2T_x$; (**c**,**f**) HRTEM images of the yellow gridlines in (**b**); (**d**,**e**) HRTEM images of the yellow gridlines in (**c**) with the insets of FFT.

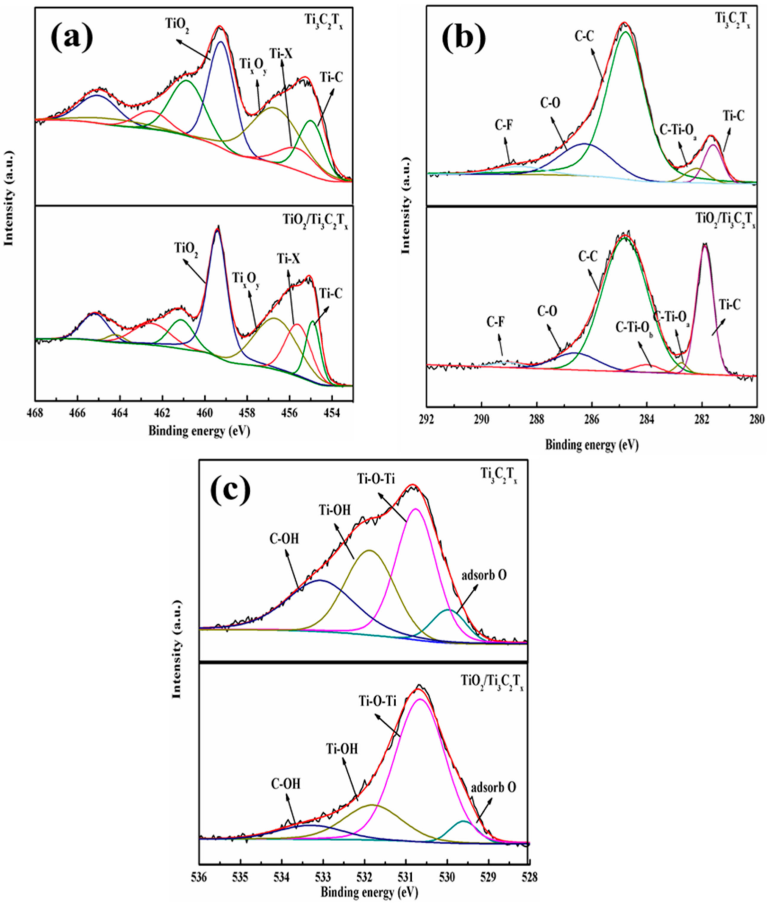

Figure 6. (**a**) Ti2p, (**b**) C1s, and (**c**) O1s XPS spectra of $Ti_3C_2T_x$ and $TiO_2/Ti_3C_2T_x$ powders.

3.2. *Characterization of Composite Coatings*

3.2.1. Compositions of Composite Coatings

XRD patterns of the Ni-P coating and the Ni–P–$TiO_2/Ti_3C_2T_x$ coating are shown in Figure 7. It is clear to see that TiO_2 and $Ti_3C_2T_x$ particles are introduced to the Ni–P–$TiO_2/Ti_3C_2T_x$ coating with these characteristic peaks of 8.95° and 25.292°, respectively. After the calcination, main phases of Ni and

Ni_3P are present in both coatings, but the peak intensity of the Ni phase increases with respect to the Ni_3P phase due to the participation of $TiO_2/Ti_3C_2T_x$ particles. In addition, $TiO_2/Ti_3C_2T_x$ particles can reduce the oriented growth of Ni, which can be determined by the following equation:

$$T = \frac{I_{(hkl)}/I_{0(hkl)}}{\sum_{i=1}^{n} I_{(hkl)}/I_{0(hkl)}} \times 100\% \tag{1}$$

where $I_{(hkl)}$ and $I_{0(hkl)}$ represent the diffraction intensity of the sample and the standard powder, respectively. In addition, n is the number of crystal planes, and T is the indices of crystal direction. As shown in Table 2, the indices of crystal direction for Ni phases in Ni–P–$TiO_2/Ti_3C_2T_x$ coatings demonstrating the T of (111) are relative high, so the oriented growth plane of Ni is (111). Thus, the addition of $TiO_2/Ti_3C_2T_x$ particles has a great effect on the composition of matrix coatings.

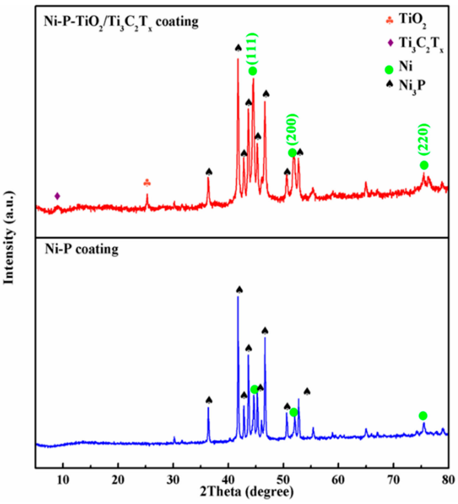

Figure 7. XRD patterns of the Ni–P coating and the Ni–P–$TiO_2/Ti_3C_2T_x$ coating.

Table 2. Crystal planes and indices of crystal direction in the Ni–P–$TiO_2/Ti_3C_2T_x$ coating.

Crystal Planes	Indices of Crystal Direction (%)
(111)	47.17
(200)	32.39
(220)	20.44

In Figure 8, a Raman spectrum of the Ni–P–$TiO_2/Ti_3C_2T_x$ coating is shown with the image of the diffraction area. From Figure 8a, the addition of $TiO_2/Ti_3C_2T_x$ makes the surface of the Ni–P–$TiO_2/Ti_3C_2T_x$ coating rough, so the $TiO_2/Ti_3C_2T_x$ particles tend to gather together on the surface. In Figure 8b, peaks of 150, 413, 520, and 634 cm^{-1} are derived from TiO_2, which corresponds to the result of Figure 3a [24]. In addition, peaks located at 1380 and 1590 cm^{-1} are assigned to D-band and G-band of $Ti_3C_2T_x$ particles. Thus, it further verifies that the Ni–P–$TiO_2/Ti_3C_2T_x$ coating is successfully prepared containing $TiO_2/Ti_3C_2T_x$ particles. In Figure 8c,d, cross-section SEM images show the thickness of Ni–P coatings and Ni–P–$TiO_2/Ti_3C_2T_x$ coatings. According to the contrast of backscattered electron imaging, the boundary between the coating and manganese steel is clear to see, so the thickness of Ni–P and Ni–P–$TiO_2/Ti_3C_2T_x$ coatings is about 10.7 and 16.3 um, respectively.

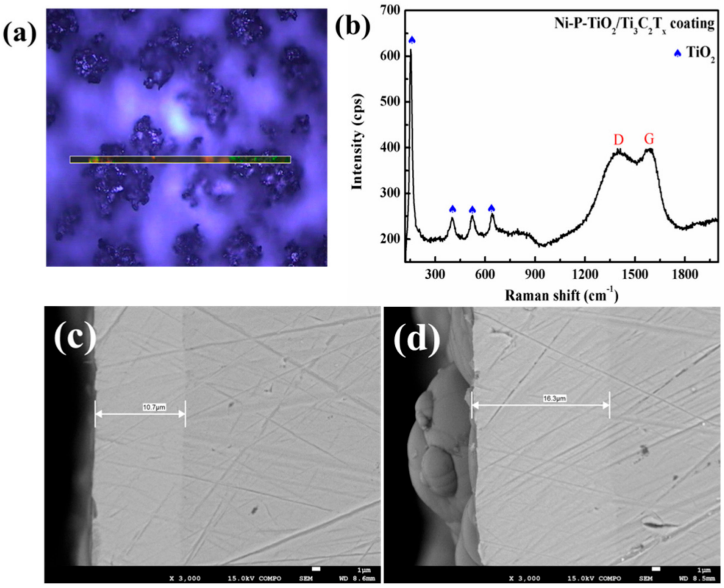

Figure 8. (**a**) Image of Raman diffraction area and (**b**) Raman spectrum of Ni–P–$TiO_2/Ti_3C_2T_x$ coatings; (**c**) and (**d**) cross-section SEM images of Ni–P coatings and Ni–P–$TiO_2/Ti_3C_2T_x$ coatings.

As shown in Figure 9, the mechanism of $TiO_2/Ti_3C_2T_x$ particles introduced into Ni–P deposits contains five steps. Cations and surfactants are absorbed into the $TiO_2/Ti_3C_2T_x$ particle to form the clouding in the bulk layer. The clouding of charged $TiO_2/Ti_3C_2T_x$ particles transfers to the cathode through a convection layer and diffusion layer, depending on electrophoresis in large part. The electrical double layer is close to the Ni–P composite coating, which is adsorbed and traps $TiO_2/Ti_3C_2T_x$ particles [6–8]. The formation of the Ni–P coating is an induced codeposition, so reduction of nickel can lead to the reduction of phosphorus, which is beneficial for the embedding and burial of $TiO_2/Ti_3C_2T_x$ particles into the Ni–P coating. Therefore, it is concluded that physical dispersion and electrophoretic migration participate in the formation of the Ni–P–$TiO_2/Ti_3C_2T_x$ coating [9]. After the calcination, Ni and Ni_3P phases can be found, which is in accordance with these results of the XRD pattern (Figure 7) and Raman spectrum (Figure 8).

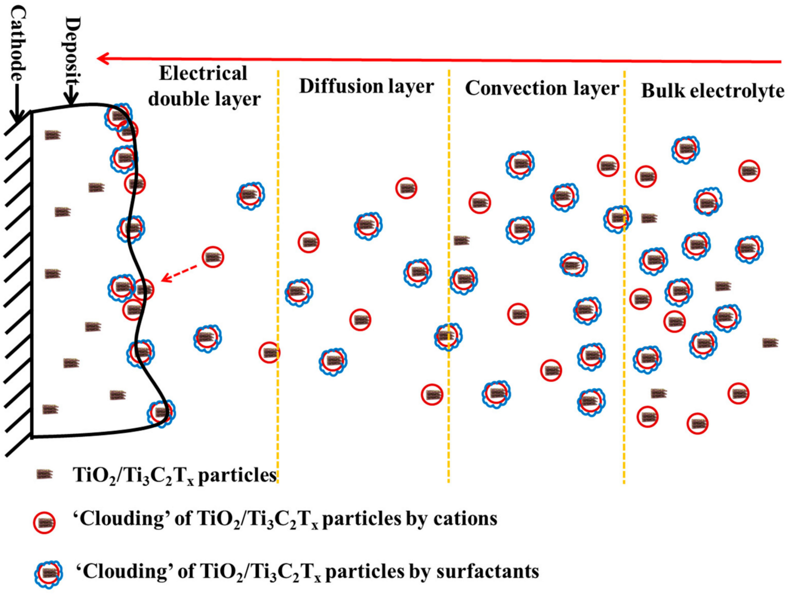

Figure 9. Mechanisms of $TiO_2/Ti_3C_2T_x$ particles' codeposition into the Ni–P deposit.

3.2.2. Wettability of Composite Coatings

Figure 10 shows SEM images of surface morphology for composite coatings and images of water drops. It is evident that the surface of Ni–P–$TiO_2/Ti_3C_2T_x$ coatings is much rougher than that of Ni–P coatings, owing to the participation of $TiO_2/Ti_3C_2T_x$ gathering on the surface. In addition, the contact angle of Ni–P–$TiO_2/Ti_3C_2T_x$ coatings is larger than that of Ni–P coatings, indicating that the addition of $TiO_2/Ti_3C_2T_x$ can lead to a change of wettability from hydrophilic to hydrophobic. It is well known that surface texture and surface energy can determine the surface wettability, which is important for the corrosion resistance of composite coatings [9]. Therefore, the gathering of $TiO_2/Ti_3C_2T_x$ on the surface and the surface roughness of the composite coating are synergistic actions for the change of wettability. The result of R_a is shown in the SEM image, so it is clear to see that the incorporation of $TiO_2/Ti_3C_2T_x$ can change the surface roughness of the Ni–P composite coating.

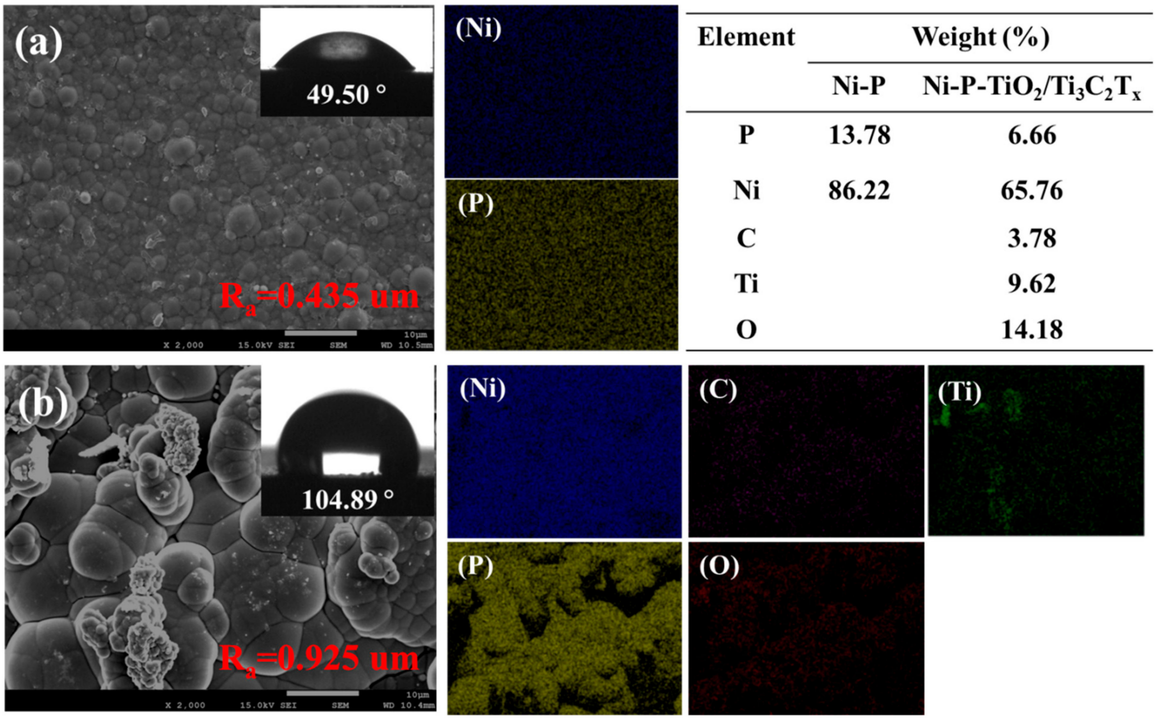

Element	Weight (%)	
	Ni-P	Ni-P-$TiO_2/Ti_3C_2T_x$
P	13.78	6.66
Ni	86.22	65.76
C		3.78
Ti		9.62
O		14.18

Figure 10. SEM images of (**a**) Ni–P coatings and (**b**) Ni–P–$TiO_2/Ti_3C_2T_x$ coatings with the EDS results (insets with images of water drops, the contact angles, and the result of R_a).

According to the EDS results, Ni and Ni_3P phases are uniformly distributed in the Ni–P coating, while these phases are aggregated partially. In addition, $TiO_2/Ti_3C_2T_x$ particles are present on the surface of Ni–P–$TiO_2/Ti_3C_2T_x$ coatings. Compared with nickel content, the incorporation of $TiO_2/Ti_3C_2T_x$ can decrease the relative content of phosphorus for Ni–P–$TiO_2/Ti_3C_2T_x$ coatings, which is likely to grow more active sites for nickel due to the existence of $TiO_2/Ti_3C_2T_x$ [19].

3.2.3. Corrosion Behavior of Composite Coatings

It is shown in Figure 11 that the electrochemical measurement is conducted at room temperature. In Figure 11a, Tafel polarization curves are processed by the Tafel extrapolation method, which can obtain the data of corrosion potential (E_{corr}), corrosion current (i_{corr}), and polarization resistance (R_p). It is obvious that the corrosion current decreases and the corrosion potential transforms to positive potential of the Ni–P coating with the addition of $TiO_2/Ti_3C_2T_x$. In addition, the polarization resistance (R_p) of the Ni–P–$TiO_2/Ti_3C_2T_x$ coating is higher than that of the Ni–P coating, confirming the improvement of corrosion protection for the Ni–P–$TiO_2/Ti_3C_2T_x$ coating. As previous papers indicated, $TiO_2/Ti_3C_2T_x$ can hinder the initiation and defect corrosion by regulating and controlling the microstructure of the composite coating [2]. Furthermore, $TiO_2/Ti_3C_2T_x$ in the Ni–P coating can form corrosion microcells, which serve as the cathode, so it promotes the anode polarization [34–36]. In addition, the passive layer can be seen in the polarization curve of Ni–P–$TiO_2/Ti_3C_2T_x$ coatings, which is good for the corrosion prevention, owing to the gathering of the $TiO_2/Ti_3C_2T_x$ on the surface and microstructure of the surface.

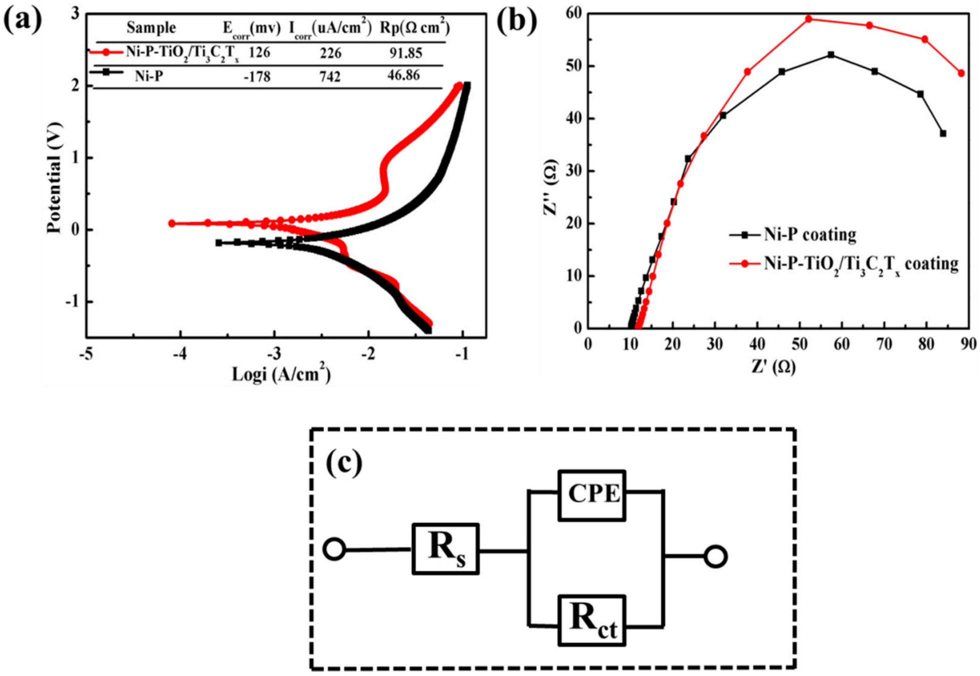

Figure 11. (**a**) The polarization curves (inset with the table of the corrosion potential (E_{corr}), corrosion current (i_{corr}), and corrosion resistance (Rp); (**b**) nyquist impedance diagrams of Ni–P and Ni–P–$TiO_2/Ti_3C_2T_x$ coatings; (**c**) equivalent circuits used for numerical fitting of impedance plots for 3.5% NaCl solution.

Nyquist impedance diagrams of Ni–P and Ni–P–$TiO_2/Ti_3C_2T_x$ coatings are shown in Figure 11b with the fitting equivalent circle model in Figure 11c, with the average error of 3.5%, which is investigated in the frequency range of 10^{-1} to 10^5. From the result of Figure 11b, it is evident that the electrochemical corrosion is mainly controlled by the diffusion process. In Figure 11c, the equivalent circuit shows the corrosion processes at the electrolyte/coatings interface. R_s stands for the solution resistance, while R_{ct}–CPE represents the charge transfer reaction, which is inversely proportional to the corrosion rate. In addition, CPE is a constant phase for a more accurate fit instead of a pure double layer capacitor. R_{ct} stands for the charge transfer resistance, so it is a measure of electron transfer across the surface. Due to the formation of nickel oxyspecies and the attack of Cl^-, a charge transfer resistor (R_{ct}) is employed to stimulate these reactions [37,38]. In Table 3, these fitting resistances of the equivalent-circuit elements contain R_s and R_{ct}. The value of R_{ct} is inversely proportional to corrosion rate. High R_{ct} of the Ni–P–$TiO_2/Ti_3C_2T_x$ coating indicates a large corrosion resistance. From these results, it is evident that the addition of $TiO_2/Ti_3C_2T_x$ can improve wear resistance of the Ni–P coating and decrease the corrosion rate, so it can be concluded that the participation of $TiO_2/Ti_3C_2T_x$ can enhance the property of corrosion prevention.

Table 3. The fitting resistances of the equivalent-circuit elements.

Sample	R_s ($\Omega\cdot cm^2$)	R_{ct} (Ω cm^2)
Ni–P coating	10.01	75.89
Ni–P–$TiO_2/Ti_3C_2T_x$ coating	13.08	87.69

3.2.4. Wear Behavior of Composite Coatings

From Figure 12, hardness and wear tests were conducted at room temperature. In Figure 12a, the fluctuation of the microhardness belonging to the Ni–P–$TiO_2/Ti_3C_2T_x$ coating is much larger than that of the Ni–P coating, highlighting the uneven surface of the Ni–P–$TiO_2/Ti_3C_2T_x$ composite coating with a high R_a for the gathering of $TiO_2/Ti_3C_2T_x$ particles on the surface of Ni–P composite coatings. In addition, the microhardness of the Ni–P coating is about 680 $kg \cdot mm^{-2}$, while that of the Ni–P–$TiO_2/Ti_3C_2T_x$ coating is approximately 1350 $kg \cdot mm^{-2}$, which is due to the dispersion strengthening and increasing grain boundaries hindering dislocation mobility [39,40]. Thus, the addition of $TiO_2/Ti_3C_2T_x$ can enhance the action of dispersion strengthening and augment grain boundaries of these composite coatings, which is beneficial for the improvement of microhardness for the composite coating.

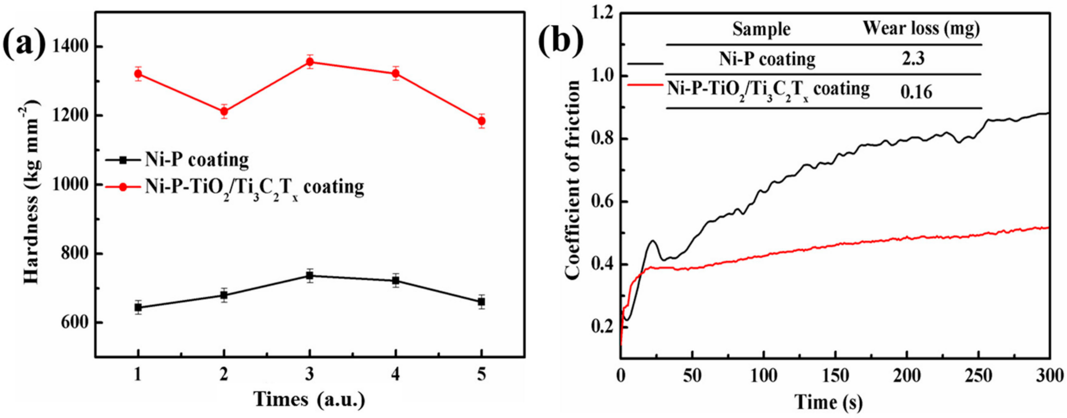

Sample	Wear loss (mg)
Ni-P coating	2.3
Ni-P-$TiO_2/Ti_3C_2T_x$ coating	0.16

Figure 12. (**a**) Microhardness and (**b**) coefficient of friction (inset with the table of wear loss) of Ni–P coatings and Ni–P–$TiO_2/Ti_3C_2T_x$ coatings.

In Figure 12b, results of the wear test are carried out under the condition of dry-grinding, accompanied with a load of 2 N, duration time of 300 s, and circle radius of 1 cm. These composite coatings and the smooth silicon nitride are taken as the stationary disk and the grinding material, respectively. The average coefficient of friction for the Ni–P coating is 0.70 after wear tests, while the average coefficient of friction for the Ni–P–$TiO_2/Ti_3C_2T_x$ coating is down to 0.40 with the participation of $TiO_2/Ti_3C_2T_x$. In addition, the table inserted in Figure 12b illustrates the wear loss after sliding tests, showing that the wear loss of Ni–P coatings and Ni–P–$TiO_2/Ti_3C_2T_x$ coatings is about 2.3 mg and 0.16 mg, respectively. As previous papers have shown, high microhardness and a low coefficient of friction can simultaneously decrease the wear loss of the Ni–P–$TiO_2/Ti_3C_2T_x$ coating [41]. Therefore, the addition of $TiO_2/Ti_3C_2T_x$ to the Ni–P coating can improve the tribological property of this coating.

4. Conclusions

In this work, in situ grown nanoparticles TiO_2 on $Ti_3C_2T_x$ sheets were prepared by a simple hydrothermal method. Taking the excellent property of TiO_2 and $Ti_3C_2T_x$ into consideration, $TiO_2/Ti_3C_2T_x$ was incorporated into the Ni–P composite coatings, which were prepared by an electroplating technique, which is little reported in this area. The following conclusions could be obtained from this study:

- The in situ grown nanocrystals TiO_2 on $Ti_3C_2T_x$ sheets can still maintain a layered structure. The Ni–P–$TiO_2/Ti_3C_2T_x$ coating is successfully prepared by an electroplating technique;
- The participation of $TiO_2/Ti_3C_2T_x$ can change the wettability of Ni–P composite coatings from hydrophilic to hydrophobic;
- The Ni–P–$TiO_2/Ti_3C_2T_x$ coating shows better properties of corrosion prevention than Ni–P coatings.

- Microhardness of the Ni–P–TiO_2/$Ti_3C_2T_x$ coating is approximately 1350 kg mm^{-2}, and the coefficient of friction of Ni–P–TiO_2/$Ti_3C_2T_x$ coatings is about 0.40, which is lower than that of the Ni–P coating.

Author Contributions: Conceptualization, Y.D., D.M., and S.Y.; Formal analysis, Y.D.; Funding acquisition, D.M. and S.Y.; Investigation, Y.D., X.Z., B.Y., and L.W.; Methodology, Y.D., X.Z., and L.W.; Supervision, D.M., Y.D., and S.Y.; Validation, Y.D. and D.M.; Writing—original draft, Y.D.; Writing—review and editing, Y.D. and S.Y.

Funding: We are thankful for the "Strategic Priority Research Program" of the Chinese Academy of Sciences (grant number XDA09040102) and National Key R and D Program of China (grant number 2016YFC0801500) for supporting this work.

Conflicts of Interest: The authors declare no conflict of interest.

References

1. Subramanian, C.; Cavallaro, G.; Winkelman, G. Wear maps for titanium nitride coatings deposited on copper and brass with electroless nickel interlayers. *Wear* **2000**, *241*, 228–233. [CrossRef]
2. Baghery, P.; Farzam, M.; Mousavi, A.B.; Hosseini, M. Ni-TiO_2 nanocomposite coating with high resistance to corrosion and wear. *Surf. Coat. Technol.* **2010**, *204*, 3804–3810. [CrossRef]
3. Zhou, Y.; Zhang, H.; Qian, B. Friction and wear properties of the co-deposited Ni-SiC nanocomposite coating. *J. Appl. Surf. Sci.* **2007**, *253*, 8335–8339. [CrossRef]
4. Hou, K.H.; Ger, M.D.; Wang, L.M.; Ke, S.T. The wear behaviour of electro-codeposited Ni-SiC composites. *Wear* **2002**, *253*, 994–1003. [CrossRef]
5. Matthews, A. *Advanced Surface Coatings: A Handbook of Surface Engineering*; Rickerby, D., Ed.; Springer: Heidelberg/Berlin, Germany, 1991; Volume 1.
6. Walsh, F.C.; Ponce de León, C. A review of the electrodeposition of metal matrix composite coatings by inclusion of particles in a metal layer: An established and diversifying coatings technology. *T.I. Met. Finish.* **2014**, *92*, 83–98. [CrossRef]
7. Wang, S.C.; Zhou, N.; Walsh, F.C. Diverse electrodeposits from modified acid sulphate (watts nickel) baths. *T.I. Met. Finish.* **2016**, *94*, 274–282. [CrossRef]
8. Zhao, G.C.; Xue, Y.; Huang, Y.; Ye, Y.; Walsh, F.C.; Chen, J.; Wang, S. One-Step electrodeposition of a self-cleaning and corrosion resistant Ni/WS_2 super hydrophobic surface. *RSC Adv.* **2016**, *6*, 59104–59112. [CrossRef]
9. He, Y.; Sun, W.T.; Wang, S.C.; Chiu, Y.L.; Reed, P.A.S.; Walsh, F.C. An electrodeposited Ni-P-WS_2 coating with combined super-hydrophobicity and self-lubricating properties. *Electrochim. Acta* **2017**, *245*, 872–882. [CrossRef]
10. Cheong, W.J.; Luan, B.L.; Shoesmeith, D.W. The effect of stabilizers on the bath stability of electroless Ni deposition and the deposit. *Appl. Surf. Sci.* **2004**, *22*, 282–300. [CrossRef]
11. Zhang, J.Y.; Xiong, D.S. Study on preparation and tribology behaviors of Ni-P electroless deposited nanocrystalline coating. *Adv. Mater. Res.* **2013**, *706*, 279–283. [CrossRef]
12. Ebn Touhami, M.; Cherkaoui, M.; Chassaing, E. Modelisation of Ni-P electroless deposition in ammonical solutions. *Electrochim. Acta* **2003**, *48*, 3651–3658. [CrossRef]
13. Antropov, L.I.; Lebedinskii, Y.N. *Composite Electrochemical Coatings and Materials*; Tekhnika: Kiev, Ukraine, 1986. (In Russian)
14. Wörle, M.; Krumeich, F.; Bieri, F.; Muhr, H.J.; Nesper, R. Flexible V_7O_{16} layers as common structural element of vanadium oxide nanotubes and a new crystalline vanadate. *Z. Anorg. Allg. Chem.* **2002**, *62*, 2778–2784. [CrossRef]
15. Volkov, S.V.; Koval'chuk, E.P.; Ohenko, V.M.; Reshetnyak, O.V. *Nanochemistry, Nanosystems, and Nanomaterials: A Monograph*; Naukova Dumka: Kiev, Ukraine, 2008. (In Ukrainia)
16. Gadhari, P.; Sahoo, P. Effect of annealing temperature and alumina particles on mechanical and tribological properties of Ni-P-Al_2O_3 composite coatings. *Silicon* **2017**, *9*, 761–774.
17. Hou, K.-H.; Hwu, W.-H.; Ke, S.-T.; Ger, M.D. Ni-P-SiC composite produced by pulse and direct current plating. *Mater. Chem. Phys.* **2006**, *100*, 54–59.

18. Naguib, M.; Kurtoglu, M.; Presser, V.; Lu, J.; Niu, J.J.; Heon, M.; Hultman, L.; Gogotsi, Y.; Barsoum, M.W. Two-Dimensional nanocrystals produced by exfoliation of Ti_3AlC_2. *Adv. Mater.* **2011**, *23*, 4248–4253. [CrossRef] [PubMed]
19. Du, Y.C.; Wang, D.D.; Si, P.C.; Wei, L.Q.; Wang, Y.L.; Yu, B.; Zhang, X.M.; Ye, S.F. Electrodeposition of a Ni-P-$Ti_3C_2T_x$/MoS_2 coating incorporating MoS_2 intercalated $Ti_3C_2T_x$ particles. *Surf. Coat. Technol.* **2018**, *354*, 119–125. [CrossRef]
20. Uttam, V.; Duchaniya, R.K. Potentiodynamic studies of Ni-P-TiO_2 nano-composited coating on the mild steel deposited by electroless plating method. *AIP Conf. Proc.* **2016**, *1725*, 020053.
21. Xu, Y.J.; Wang, S.; Yang, J.; Han, B.; Nie, R.; Wang, J.X.; Wang, J.G.; Jing, H.W. In-Situ grown nanocrystal TiO_2 on 2D Ti_3C_2 nanosheets for artificial photosynthesis of chemical fuels. *Nano Energy* **2018**, *51*, 442–450. [CrossRef]
22. Peng, C.; Yang, X.F.; Li, Y.H.; Yu, H.; Wang, H.J.; Peng, F. Hybrids of two-dimensional Ti_3C_2 and TiO_2 exposing {001} facets toward enhanced photocatalytic activity. *ACS Appl. Mater. Interfaces* **2016**, *8*, 6051–6060. [CrossRef] [PubMed]
23. Zheng, M.; Guo, R.S.; Liu, Z.C.; Wang, B.Y.; Meng, L.C.; Li, F.Y.; Li, T.T.; Luo, Y.N. MoS_2 intercalated p-Ti_3C_2 anode materials with sandwich-like three dimensional conductive networks for lithium-ion batteries. *J. Alloys Compd.* **2018**, *735*, 1262–1270. [CrossRef]
24. Naguib, M.; Presser, V.; Tallman, D.; Lu, J.; Hultman, L.; Gogotsi, Y.; Barsoum, M.W. On the topotactic transformation of Ti_2AlC into a Ti-C-O-F cubic phase by heating in molten lithium fluoride in air. *J. Am. Ceram. Soc.* **2011**, *94*, 4556–4561. [CrossRef]
25. Naguib, M.; Mashtalir, O.; Carle, J.; Presser, V.; Lu, J.; Hultman, L.; Gogotsi, Y.; Barsoum, M.W. Two-dimensional transition metal carbides. *ACS Nano* **2012**, *6*, 1322–1331. [CrossRef] [PubMed]
26. Bricchi, B.R.; Ghidelli, M.; Mascaretti, L.; Zapelli, A.; Russo, V.; Casari, C.S.; Terraneo, G.; Alessandri, I.; Ducati, C.; Bassi, A.L. Integration of plasmonic Au nanoparticles in TiO2 hierarchical structures in a single-step pulsed laser co-deposition. *Mat. Des.* **2018**, *156*, 311–319.
27. Xue, M.Q.; Wang, Z.Q.; Yuan, F.; Zhang, X.H.; Wei, W.; Tang, H.; Li, C.S. Preparation of TiO_2/$Ti_3C_2T_x$ hybrid nanocomposites and their tribological properties as base oil lubricant additives. *RSC Adv.* **2017**, *7*, 4312–4319. [CrossRef]
28. Yang, H.G.; Sun, C.H.; Qiao, S.Z.; Zou, J.; Liu, G.; Smith, S.C.; Cheng, H.M.; Lu, G.Q. Anatase TiO_2 single crystals with a large percentage of reactive facets. *Nature* **2008**, *453*, 638–641. [CrossRef] [PubMed]
29. Zhang, J.; Xi, J.; Ji, Z. Mo+N codoped TiO_2 sheets with dominant {001} facets for enhancing visible-light photocatalytic activity. *J. Mater. Chem.* **2012**, *22*, 17700–17708. [CrossRef]
30. Yang, X.; Zhuang, J.; Li, X.; Chen, D.; Ouyang, G.; Mao, Z.; Han, Y.; He, Z.; Liang, C.; Wu, M.; et al. Hierarchically nanostructured rutile arrays: Acid vapor oxidation growth and tunable morphologies. *ACS Nano* **2009**, *3*, 1212–1218. [CrossRef] [PubMed]
31. Lai, Z.; Peng, F.; Wang, Y.; Wang, H.; Yu, H.; Liu, P.; Zhao, H. Low temperature solvothermal synthesis of anatase TiO_2 single crystals with wholly {100} and {001} faceted surfaces. *J. Mater. Chem.* **2012**, *22*, 23906–23912. [CrossRef]
32. Rakhi, R.B.; Ahmed, B.; Hedhili, M.N.; Anjum, D.H.; Alshareef, H.N. Effect of postetch annealing gas composition on the structural and electrochemical properties of $Ti_3C_2T_x$ MXene electrodes for super capacitor applications. *Chem. Mater.* **2015**, *27*, 5314–5323. [CrossRef]
33. Li, B.; Zhao, Z.; Gao, F.; Wang, X.; Qiu, J. Mesoporous microspheres composed of carbon-coated TiO_2 nanocrystals with exposed {001} facets for improved visible light photocatalytic activity. *Appl. Catal. B* **2014**, *147*, 958–964. [CrossRef]
34. Abdel Aal, A. Hard and corrosion resistant nanocomposite coating for Al alloy. *J. Mater. Sci. Eng. A* **2008**, *474*, 181–187. [CrossRef]
35. Chen, X.H.; Chen, C.S.; Xiao, H.N.; Cheng, F.Q.; Zhang, G.; Yi, G.J. Corrosion behavior of carbon nanotubes-Ni composite coating. *Surf. Coat. Technol.* **2005**, *191*, 351–356. [CrossRef]
36. Abdel-Gabar, A.M.; Abd-El-Nabey, B.A.; Sidahmed, I.M.; El-Zayady, A.M.; Saadawy, M. Inhibitive action of some plant extracts on the corrosion of steel in acidic media. *J. Corros. Sci.* **2006**, *48*, 2765–2779. [CrossRef]
37. Wang, L.; Zhang, J.; Gao, Y.; Xue, Q.; Hu, L.; Xu, T. Grain size effect in corrosion behavior of electrodeposited nanocrystalline Ni coatings in alkaline solution. *J. Scripta Mater.* **2006**, *55*, 657–660. [CrossRef]

38. Bai, A.; Chuan, P.Y.; Hu, C.C. The corrosion behavior of Ni-P deposits with high phosphorous contents in brine media. *J. Mater. Chem. Phys.* **2003**, *82*, 93–100. [CrossRef]
39. Czagány, M.; Baumli, P.; Kaptay, G. The influence of the phosphorous content and heat treatment on the nano-micro-structure, thickness and micro-hardness of electroless Ni-P coatings on steel. *Appl. Surf. Sci.* **2017**, *423*, 160–169. [CrossRef]
40. Matteo, G.; Marco, S.; Christian, C.; Raphael, G. Determination of the elasticmoduli and residual stresses of freestanding Au-TiW bilayer thin films by nanoindentation. *Mat. Des.* **2016**, *106*, 436–445.
41. He, Y.; Wang, S.C.; Walsh, F.C.; Chiu, Y.L.; Reed, P.A.S. Self-Lubricating Ni-P-MoS_2 composite coatings. *Surf. Coat. Technol.* **2016**, *307*, 926–934. [CrossRef]